npj Flexible Electronics

https://doi.org/10.1038/s41528-026-00622-9

Article in Press

A skin-adhesive bimodal sensing patch for occlusal function assessment

Received: 25 March 2026

Accepted: 13 July 2026

Published online: 22 July 2026

Cite this article as: Huang, L., Li, R., Li, X. *et al.* A skin-adhesive bimodal sensing patch for occlusal function assessment. *npj Flex Electron* (2026). https://doi.org/10.1038/s41528-026-00622-9

Longchao Huang, Ruoxi Li, Xuelan Li, Yue Sun, Shenglong Wang, Boling Lan, Guanfa Li, Long Jin, Wei Zhu, Weiqing Yang & Weili Deng

We are providing an unedited version of this manuscript to give early access to its findings. Before final publication, the manuscript will undergo further editing. Please note there may be errors present which affect the content, and all legal disclaimers apply.

If this paper is publishing under a Transparent Peer Review model then Peer Review reports will publish with the final article.

ARTICLE IN PRESS

© The Author(s) 2026. **Open Access** This article is licensed under a Creative Commons Attribution-NonCommercial-NoDerivatives 4.0 International License, which permits any non-commercial use, sharing, distribution and reproduction in any medium or format, as long as you give appropriate credit to the original author(s) and the source, provide a link to the Creative Commons licence, and indicate if you modified the licensed material. You do not have permission under this licence to share adapted material derived from this article or parts of it. The images or other third party material in this article are included in the article's Creative Commons licence, unless indicated otherwise in a credit line to the material. If material is not included in the article's Creative Commons licence and your intended use is not permitted by statutory regulation or exceeds the permitted use, you will need to obtain permission directly from the copyright holder. To view a copy of this licence, visit http://creativecommons.org/licenses/by-nc-nd/4.0/.

ARTICLE IN PRESS

A Skin-Adhesive Bimodal Sensing Patch for Occlusal Function Assessment

*Longchao Huang[1, †], Ruoxi Li[2, †], Xuelan Li[1], Yue Sun[1], Shenglong Wang[1], Boling Lan[1], Guanfa Li[1], Long Jin[1], Wei Zhu[3, *], Weiqing Yang[1,4, *], Weili Deng[1, *]*

[1] Key Laboratory of Advanced Technologies of Materials (Ministry of Education), School of Materials Science and Engineering, Southwest Jiaotong University, Chengdu 610031, P. R. China

[2] Institute of Biomedical Engineering College of Medicine, Southwest Jiaotong University, Chengdu 610031, P. R. China

[3] School of Energy and Power Engineering, Nanjing University of Science and Technology, Nanjing 210094, P. R. China

[4] Research Institute of Frontier Science, Southwest Jiaotong University, Chengdu 610031, P. R. China

[†] These authors contributed equally to this work

* Corresponding author: weili1812@swjtu.edu.cn; zhuwei@njust.edu.cn; wqyang@swjtu.edu.cn

ARTICLE IN PRESS

Abstract

Occlusal dysfunction is a prevalent orofacial disorder characterized by aberrant occlusal force transmission and dysregulated masticatory muscle activity. Currently, quantitative characterization of occlusion-related neuromechanical activity remains challenging in clinical practice. In this study, we propose a skin-interfaced bimodal sensing patch that integrates serpentine-structured piezoelectric poly(vinylidene fluoride) (PVDF) films with conductive hydrogel electrodes for simultaneous monitoring of facial skin deformation and muscle electrophysiology during occlusal activities. The island-serpentine design ensures high mechanical compliance while preserving stable electromechanical performance over more than 12,000 loading cycles. The hydrogel interface serves not only as an adhesive layer enabling conformal adhesion of the PVDF film to the skin but also functions as a low-impedance electrode, facilitating high-fidelity surface electromyography (sEMG) with a signal-to-noise ratio of ~30 dB. Through combined analysis of

ARTICLE IN PRESS

piezoelectric and sEMG signals, the system distinguishes distinct functional occlusal actions, including normal occlusion, deep overbite, crossbite, and mandibular deviation. This bimodal framework provides a preliminary proof-of-concept for multimodal functional characterization of occlusal biomechanics and suggests potential applicability in noninvasive occlusal function assessment.

Keywords: serpentine PVDF, coated hydrogel, bimodal sensor, malocclusion classification

Introduction

Occlusal dysfunction is a highly prevalent functional disorder of the orofacial system and is widely recognized as an important risk factor for temporomandibular disorders (TMD).[1-3] TMD, a broad term encompassing various disorders affecting the temporomandibular joint and its surrounding muscles, has a reported prevalence of approximately 10-20% in the general population, with many individuals experiencing symptoms such as pain, limited jaw movement, and muscular dysfunction that considerably impair quality of life.[4] Characterized by abnormal occlusal contact and masticatory muscle activation, occlusal dysfunction frequently co-occurs with TMD and often exacerbates symptoms, thereby increasing clinical complexity.

Its clinical presentations, often associated with malocclusion patterns, such as deep overbite, crossbite, and mandibular deviation, frequently involve imbalanced occlusal force transmission, abnormal masticatory muscle activation, and elevated loading of the temporomandibular joint.[5, 6] From a biomechanical perspective, occlusal function is governed not only by static structural factors (e.g., tooth contacts, mandibular kinematics and craniofacial morphology) but also by dynamic functional parameters, including the distribution of occlusal forces and patterns of masticatory muscle activation. Current clinical assessments mostly rely on oral examinations, dental cast analysis, medical imaging, or isolated bite force measurements. While invaluable for structural diagnosis, these methods fall short in capturing the dynamic interplay between

ARTICLE IN PRESS

neuromuscular activity and force transmission during natural mastication.[7-10]

Recent advances in wearable flexible electronics have opened new possibilities for noninvasive monitoring of orofacial functions.[11-15] Prior work has employed various sensing mechanisms, including piezoelectric,[16-21] piezoresistive,[22-24] capacitive,[6, 25] electromagnetic,[26, 27] electromyographic,[28-31] iontronic[32, 33]and photoelectric transduction,[34, 35] to quantify masticatory muscle activity or occlusal behavior. Among these modalities, piezoelectric sensing is particularly suitable for capturing dynamic skin deformation and transient mechanical responses during mastication, whereas sEMG directly reflects neuromuscular activation. Their integration thus provides complementary mechanical and electrophysiological information that cannot be obtained by single-modality sensing alone. These combined approaches introduce continuous, objective perspectives into functional assessment. In particular, skin-mounted flexible sensors, due to their wearing comfort and mechanical adaptability, are well-suited for monitoring in complex facial regions.[36-39]

However, masticatory function involves significant skin deformation, pronounced muscle contraction, and multiaxial mechanical loading, which collectively impose stringent demands on sensor compliance, signal stability, and long-term durability.[40-42] Current flexible thin-film devices often struggle to achieve both conformal attachment and stable fixation on curved non-structured skin surfaces.[43, 44] In the absence of reliable interfacial adhesive layers, such devices often rely on additional medical tapes for fixation, which can introduce mechanical interference and compromise signal consistency.[45-49] Furthermore, single-modality sensing fails to capture the coordinated neuromechanical mechanisms underlying occlusal function.[50, 51] Consequently, there is a clear need for a multimodal, flexible sensing patch capable of conforming to complex facial topography, maintaining stable skin adhesion, and supporting long-term monitoring.

Here, we present a wearable, noninvasive, and highly conformal bimodal flexible sensor patch

ARTICLE IN PRESS

for in situ recording of occlusion-related facial skin deformation and muscle electrophysiology. The device integrates a serpentine-structured poly(vinylidene fluoride) (PVDF) piezoelectric film with a conductive hydrogel layer, achieving high flexibility for adaptation to complex orofacial curvature while preserving stable piezoelectric performance and conductivity. The island-serpentine architecture effectively alleviates stress concentration, enabling precise tracking of surface deformation via the piezoelectric output. Beyond ensuring conformal adhesion, the conductive hydrogel layer exhibits favorable electrical properties and concurrently functions as a surface electromyography (sEMG) electrode to capture muscle activity signals. Through combined analysis of piezoelectric and sEMG signals, this patch demonstrates a preliminary framework for multimodal occlusal action classification.

Results

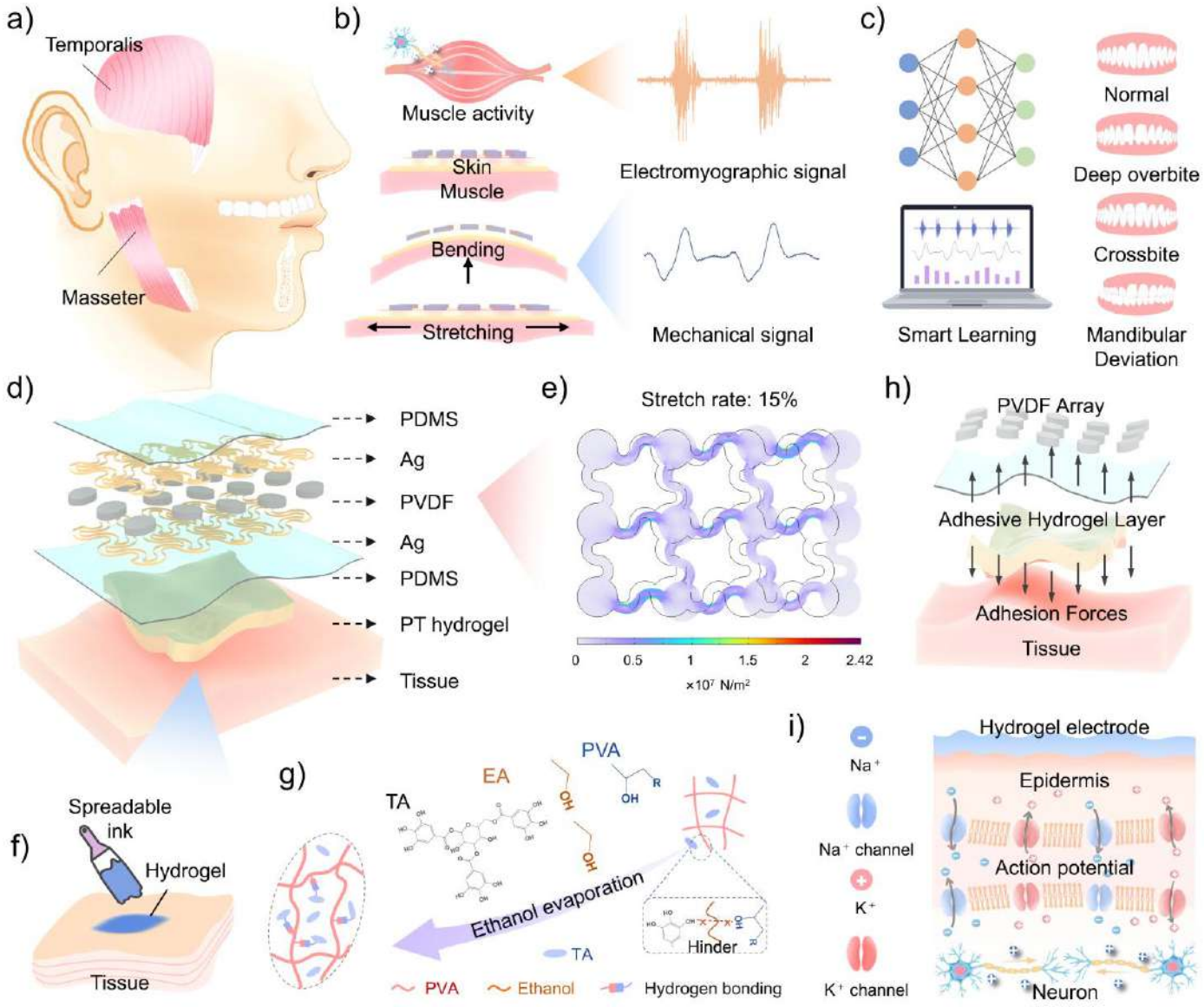
Design Principles for Dual-Mode Sensors for Occlusal Monitoring

The masseter muscle serves as the primary driver of occlusal forces during mastication,[2, 52] while the temporalis muscle stabilizes the mandibular bone and contributes to the occlusal dynamics (**Fig. 1a**). Accurate quantification of these muscle activities is crucial for assessing occlusal function. To capture the muscle dynamics associated with occlusion, we developed a bimodal sensing strategy that concurrently records sEMG and piezoelectric signals. The sEMG electrodes detect electrophysiological activity during muscle contraction and relaxation, while the piezoelectric layer synchronously monitors dynamic mechanical deformations of facial tissues (**Fig. 1b**). A machine learning framework processes this fused data to classify different occlusal states, including normal occlusion, deep overbite, crossbite, and mandibular deviation (**Fig. 1c**). The architecture of the bimodal sensor patch is illustrated in **Fig. 1d**, where the piezoelectric component features an island-bridge-structured poly(vinylidene fluoride) (PVDF) film, offering both mechanical stretchability and conformance to complex facial contours, thus enabling precise

ARTICLE IN PRESS

capture of local tissue strains. Biomechanical studies indicate that facial skin-surface deformation induced by mandibular or temporomandibular joint functional movements is typically on the millimeter scale. Specifically, average deformations range from 0.31 to 1.62 mm, with a maximum depression of approximately 3.26 mm during mouth opening.[53-55] For a device with a length of 25 mm, this physiological motion translates to a global deformation of approximately 10 to 15%. To accommodate this biological requirement, we evaluated the mechanical behavior of the patch under a 15% global tensile strain (**Fig. 1e**). The local strain and stress distributions are highly non-uniform due to the island–serpentine layout. The mechanical loads are mainly redistributed along the serpentine interconnects, while the island regions remain relatively protected. The sEMG electrodes are fabricated by depositing liquid hydrogel ink followed by a controlled drying process (**Fig. 1f**). As depicted in **Fig. 1g**, solvent evaporation induces hydrogen bonding, leading to gelation and forming a strongly adhesive interface with the skin. This design not only facilitates mechanical coupling between the piezoelectric layer and the skin (**Fig. 1h**) but also enables the hydrogel electrode to efficiently collect sEMG signals from the skin surface (**Fig. 1i**). These combined features underscore the potential of this bimodal sensing platform for long-term, noninvasive bioelectrical monitoring.

ARTICLE IN PRESS



To capture non-structural mechanical deformations of the facial surface, we designed a piezoelectric film with an island–serpentine structure for conformal attachment to curved skin. The device was fabricated by electrospinning PVDF into highly aligned nanofibers, followed by hot-pressing and laser patterning to define the serpentine geometry (**Fig. 2a**). During processing, the combined electrical, thermal, and mechanical fields precisely regulated the crystallization of PVDF, promoting the formation of the electroactive β-phase.[13, 20] This integrated fabrication route yielded a film with both high piezoelectric activity and exceptional mechanical compliance, enabling it to conform closely to curved substrates (**Fig. 2b**). To ensure reliable electrical

ARTICLE IN PRESS

connection with external circuitry, a single-sided electrode was reserved on one edge of the film to serve as the contact terminal (**Fig. S1**).

Serpentine-structured piezoelectric PVDF films

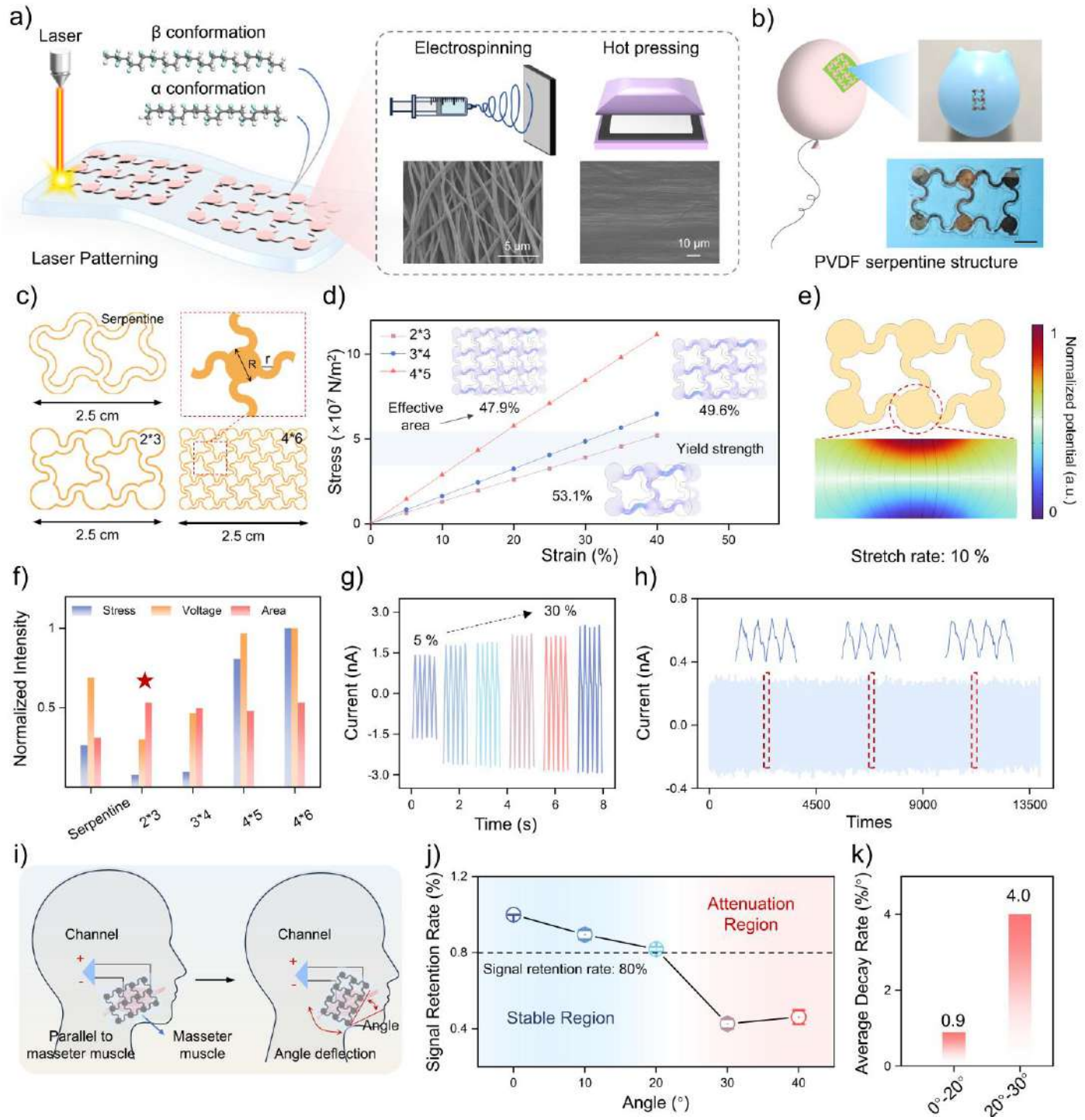
Finite element analysis was employed to optimize the device geometry by analyzing the stress distribution, strain accommodation, and electrical output across different spatial densities (**Fig. 2c** and **S2a-c**). The serpentine interconnects effectively redistributed the global tensile strain to maintain overall elasticity, while the island regions served as mechanically stable piezoelectric sensing units. Simulation results indicate that the 2 × 3 configuration reached the typical yield strength of the PVDF film (approximately 35–55 MPa) only when the global strain reached 40%, and even the 4 × 5 configuration required a global strain of 19% to reach this stress threshold (**Fig. 2d** and **S2d-e**). Given that the actual monitoring strain is typically below 15%, the designed configurations maintain sufficient mechanical margins to satisfy the durability requirements for repeated facial occlusion-monitoring applications. Notably, the piezoelectric potential was predominantly localized within the island regions (**Fig. 2e**), indicating that the serpentine bridge structure effectively decoupled mechanical deformation from electrical transduction while preserving robust signal output.

Given that facial motion involves coupled global tensile strain and normal pressure, the effective sensing area represents a critical design parameter. However, as unit density increases, the overall effective working area of the entire device gradually decreases. Through a systematic evaluation of voltage output, mechanical stress, and sensing coverage (**Fig. 2f**), the 2 × 3 unit configuration was identified as the optimal design, balancing signal fidelity, mechanical compliance, and fabrication efficiency. Electromechanical characterization revealed that output current increased with applied global tensile strain, exhibiting two distinct linear regimes (**Fig. 2g**). Higher sensitivity was observed at strains below 10%, attributed to non-uniform stress

ARTICLE IN PRESS

redistribution within the island–bridge structure during initial deformation **(Fig. S3**). To evaluate physiological relevance, the device was tested under conditions mimicking human masseter muscle activity, with a typical mastication frequency of 60–120 times per minute. When stretched at 30% strain at a frequency of 2 Hz, the device produced output voltages of approximately 0.5 V **(Fig. S4**). The device also demonstrated decent mechanical durability, with negligible signal degradation after about 14,000 stretching cycles (**Fig. 2h**). Angular-dependent measurements were performed to assess tolerance to placement misalignment. As shown in **Fig. 2i-k**, the device maintained stable performance within a misalignment range of 0–20°, with signal retention exceeding 80%. The signal decay rate remains as low as 0.9% per degree within 0–20°, and increases to 4.0% per degree in the 20°-30° range. These results provide preliminary validation of the reliability of the serpentine PVDF film structure for the repeated dynamic monitoring of facial mechanical deformation.

ARTICLE IN PRESS



Preparation and performance characterisation of coatable hydrogel bioelectrodes

As shown in **Fig. 3a,** the hydrogel ink is formulated from poly(vinyl alcohol) (PVA) and tannic acid (TA). PVA serves as the primary hydrogel matrix owing to its biocompatibility, low cost, and excellent film-forming ability, while TA introduces a dense hydrogen-bonded network that

ARTICLE IN PRESS

enhances stretchability. Aluminum chloride hexahydrate provides ionic conductivity and facilitates ion-mediated crosslinking, whereas glycerol forms extensive hydrogen bonds with water, thereby improving water retention.

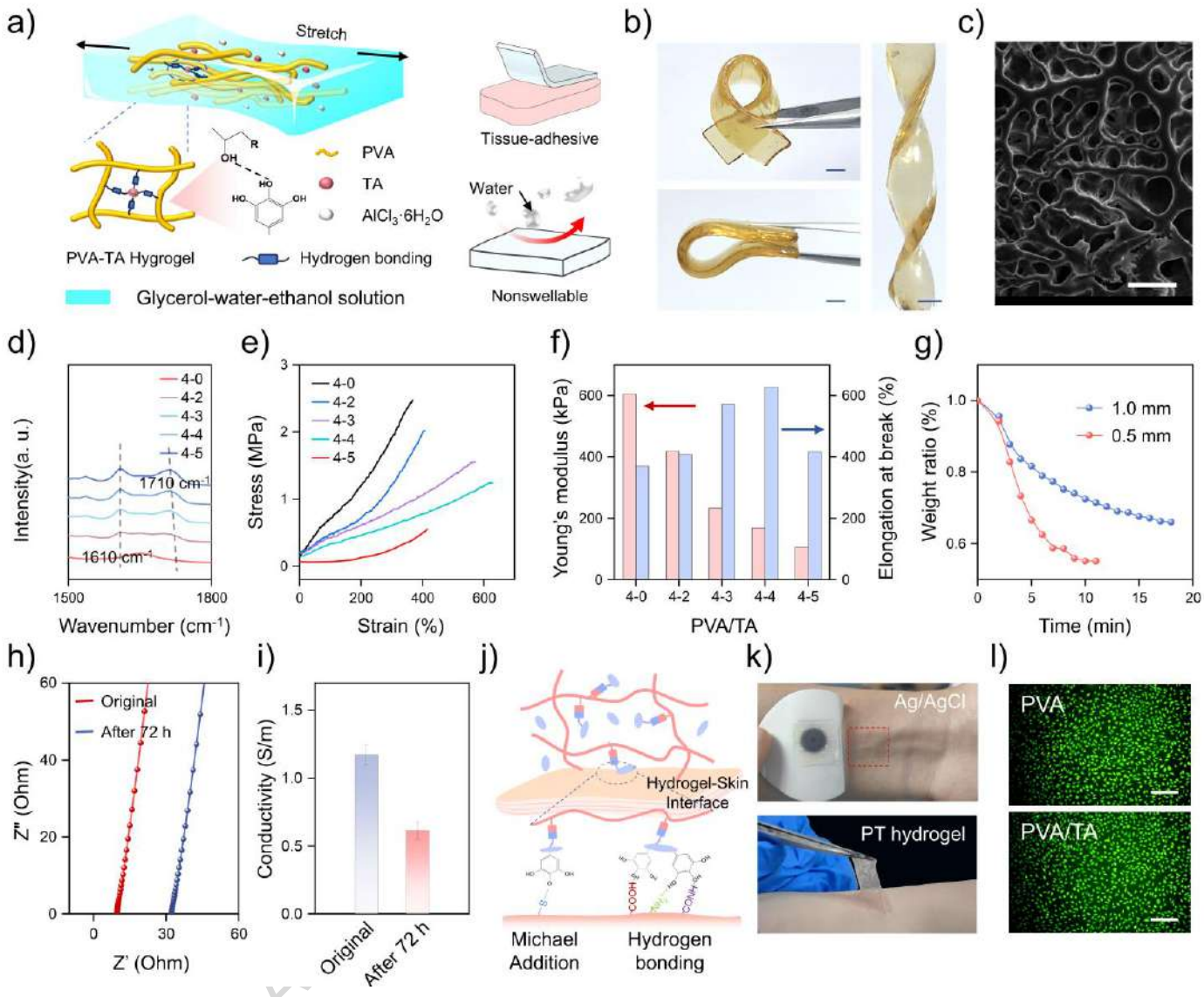
To maintain ink fluidity and prevent premature gelation, competitive hydrogen-bond interactions between the solvents and solutes must be finely regulated.[56-58] Water strongly solvates the hydroxyl groups of PVA, whereas ethanol preferentially interacts with the phenolic hydroxyl groups in TA. These competitive solvent–solute interactions effectively suppress direct PVA–TA association, stabilizing the ink and preventing early network formation. Following skin application, the elevated local temperature accelerates ethanol evaporation, enabling reformation of hydrogen-bonded PVA–TA networks and resulting in a robust structure. By adjusting TA content, we tuned the rheological and mechanical properties of the PVA/TA (PT) hydrogel inks, obtaining a series of formulations with distinct gelation behaviors (**Tables S1-S2** and **Fig. S5)**. To demonstrate the mechanical properties of the hydrogel, we prepared a transparent, pale-yellow hydrogel with substantial thickness using a multi-layer casting process, which exhibited good flexibility (**Fig. 3b**). The scanning electron microscopy (SEM) image reveals a dense, interconnected porous microstructure that contributes to both mechanical integrity and ionic conductivity (**Fig. 3c**). Fourier-transform infrared spectroscopy (FTIR) spectra confirm structural evolution induced by TA incorporation (**Fig. 3d** and **S6**). New absorption bands at 1710 and 1610 cm^{-1} correspond to C=O stretching and aromatic C=C vibrations, respectively, validating the successful integration of TA into the PVA network. Increasing TA content induced a slight red shift of the C=O band, indicating that carbonyl groups act as hydrogen-bond acceptors in PVA–TA interactions, which lowers the force constant of the C=O bond. Compared with pristine PVA, PT hydrogels also display a stronger crystallization peak at ≈19–20° in XRD profiles, suggesting that TA promotes chain ordering through hydrogen bonding and enhances crystallinity (**Fig. S7**).

ARTICLE IN PRESS

Mechanical testing of PT hydrogels with different compositions (**Fig. 3e**) revealed that a PVA: TA mass ratio of 4:4 yields optimal performance, achieving a high fracture strain of 627% and a skin-compatible modulus of 0.16 MPa (**Fig. 3f**).

To evaluate the potential of PT hydrogels as long-term sEMG bioelectrodes, we further investigated their stability, electrical properties, and adhesion. As shown in **Fig. 3g**, when applied at near-skin temperature (≈30 °C), rapid ethanol evaporation enables the hydrogel to form a uniform, conformal film. Electrochemical impedance spectroscopy (**Fig. 3h** and **S8**) shows that the hydrogel exhibits an initial ionic conductivity of 1.17 S m^{-1}, and 0.62 S m^{-1} after 72 h, which is sufficient for stable biopotential recording (**Fig. 3i**). To further evaluate the on-skin electrode interface, the electrode-skin contact impedance of the PT hydrogel electrode was measured and compared with that of commercial Ag/AgCl electrodes. The PT hydrogel electrode exhibited lower impedance over the measured frequency range, indicating a favorable low-impedance interface for sEMG signal acquisition (**Fig. S9**). Furthermore, the free catechol groups in TA can form hydrogen bonds and Michael additions at the PT bio-hydrogel/skin interface. Combined with ionic interactions, these mechanisms create a durable hydrogel-skin interface, as illustrated in **Fig. 3j**. In comparison with commercial electrodes, the PT hydrogel exhibits skin-friendliness, adhesion, and patterning flexibility, enabling stable attachment to skin and various object surfaces (**Fig. 3k** and **S10-11**). Live/dead assays confirm that both TA-containing and TA-free PVA hydrogels show negligible cytotoxicity toward fibroblasts (**Fig. 3l** and **S12**). Notably, the hydrogel also adheres strongly to non-biological substrates, ensuring mechanical integrity between the piezoelectric and sEMG layers in multimodal sensing patches.

ARTICLE IN PRESS



As shown in **Fig. 4a**, the sEMG and piezoelectric electrodes were attached to the masseter muscle, with the forehead serving as a reference electrode for analyzing muscle activity under different simulated occlusal states (**Fig. S13**). The task design was intended to mimic representative occlusal-action patterns that may involve different masseter activation and facial skin-surface deformation responses. Specifically, normal occlusion, crossbite-like, deep-overbite-like, and mandibular-deviation-like actions were simulated to generate task-dependent electrophysiological and mechanical signal features. The conductive copper wires were embedded within the hydrogel through multiple coating layers, with the piezoelectric layer adhered on top

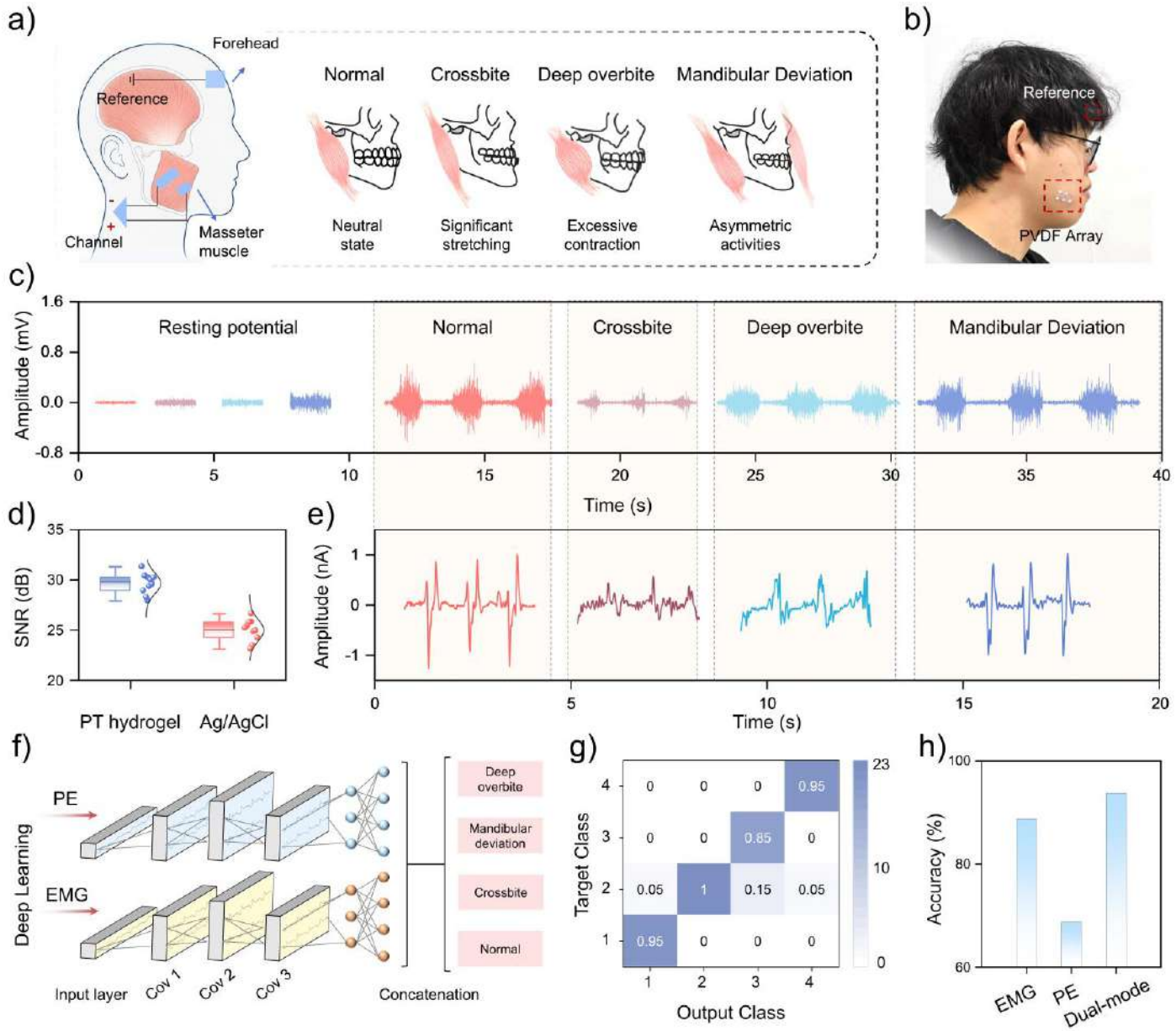
ARTICLE IN PRESS

(**Fig. 4b** and **S14**).

Recognition and classification of occlusal motions

To decode the complex neuromuscular and skin-deformation patterns associated with occlusal dysfunction, we developed a bimodal dataset that integrates sEMG and epidermal piezoelectric sensing. As shown in **Fig. 4c**, different simulated occlusal tasks produced distinguishable sEMG waveform patterns, including variations in baseline level, signal amplitude, waveform duration, and bilateral signal distribution (**Fig. S15**). In terms of signal fidelity, PT hydrogel electrodes demonstrated a superior signal-to-noise ratio (SNR) of approximately 30 dB, notably higher than commercial Ag/AgCl electrodes (around 25 dB) under identical testing conditions (**Fig. 4d** and **S16**). The piezoelectric signals were synchronized with mechanical deformations, suggesting that the piezoelectric responses reflected task-related mechanical deformation coupled with muscle activation (**Fig. 4e**). To leverage these complementary spatiotemporal features for precise occlusal classification, we designed a customized dual-stream convolutional neural network (CNN) (**Fig. 4f**). The fusion model achieved a classification accuracy of 93.75%, significantly outperforming single-modality inputs (**Fig. 4g-h** and **S17-S19**). These results demonstrate the preliminary feasibility of combining epidermal piezoelectric sensing and sEMG recording for personalized classification of occlusal actions.

ARTICLE IN PRESS



Discussion

In summary, we developed a skin-interfaced bimodal sensing platform that integrates PVDF-based dynamic deformation sensing with hydrogel-based surface electromyography for occlusion-related functional monitoring. By combining a mechanically compliant island-serpentine PVDF architecture with an adhesive and conductive hydrogel interface, the system enables repeated dynamic recording of occlusion-related skin-surface deformation and masticatory muscle activation under the tested conditions. Through bimodal signal fusion, this approach enables

ARTICLE IN PRESS

personalized quantitative classification of selected simulated occlusal-action patterns, providing preliminary proof-of-concept evidence for combining epidermal piezoelectric sensing with sEMG recording in occlusion-related neuromechanical analysis. This work establishes a noninvasive framework for functional occlusion monitoring and highlights the broad prospects of bimodal epidermal sensors in orofacial biomechanics.

Methods

Materials

Polyvinyl alcohol (PVA, 1799), tannic acid (TA), glycerol, ethanol, aluminum chloride hexahydrate ($AlCl_3 \cdot 6H_2O$), *N, N*-dimethylformamide (DMF), and acetone were purchased from Aladdin Reagent Co., Ltd. Polyvinylidene fluoride (PVDF) was obtained from Piezo Technologies (France). All chemicals were used as received without further purification.

Fabrication of piezoelectric PVDF films

PVDF precursor solution (0.15 g mL^{-1}) was prepared by dissolving PVDF powder in a DMF/acetone mixed solvent (2:1, v/v) under continuous stirring at 50 °C overnight. Aligned PVDF nanofibers were fabricated by electrospinning at a voltage of 10 kV with a working distance of 10 cm onto a high-speed rotating drum collector (1500 rpm).

To enhance crystallinity and mechanical robustness, the as-spun nanofiber mats were hot-pressed at 160 °C for 30 min, yielding dense and uniform films. A serpentine geometry was fabricated via laser ablation to endow the film with structural stretchability. An intact region was intentionally preserved along one edge as an electrical terminal (Fig. S1). Silver electrodes were then deposited by vacuum evaporation, forming double-sided electrodes on the serpentine region and a single-sided electrode on the terminal pad. Electrical interconnection was achieved by attaching copper/conductive carbon cloth leads to the terminal electrode. Electrical poling was performed using an arbitrary waveform generator (TBS1104, Tektronix) coupled with a high-

ARTICLE IN PRESS

voltage amplifier (ATA7030, Aigtek). The final flexible piezoelectric active layer was encapsulated by PDMS, forming a PDMS-PVDF-PDMS sandwich structure.

Preparation of PT hydrogel electrodes

PVA, TA, and $AlCl_3 \cdot 6H_2O$ were dissolved in 10 mL of a mixed solvent (glycerol/water/ethanol = 3:4:5, v/v) and stirred at 70 °C for 3-4 h until a homogeneous solution was obtained.[57] After degassing in a water bath to remove trapped bubbles, a uniformly dispersed PT hydrogel ink was formed. Hydrogel films were prepared by coating, with thickness precisely controlled via a layer-by-layer deposition process.

Assembly of the multilayer device

After application of the hydrogel ink to the skin surface, ethanol evaporation promotes hydrogen bond formation between the two phases, causing the hydrogel to cure over approximately 10 minutes. To ensure better adhesion between the piezoelectric layer and the electromyographic electrode layer, copper wire embedding and interlayer assembly were performed during the curing process of approximately 7 minutes. The entire device has overall dimensions of 2.5 cm × 1.6 cm, with a hydrogel layer thickness of 0.5 mm, a PVDF piezoelectric layer of approximately 30 μm, and a PDMS layer of approximately 10 μm.

ARTICLE IN PRESS

Materials and devices characterization

The chemical structures and crystal structures were determined by Fourier transform infrared spectroscopy (FTIR, Nicolet IS50 spectrometer) and X-ray diffraction (XRD, DX-1000 diffractometer), respectively. Surface topography was characterized by scanning electron microscopy (SEM, JEOL JSM7800F). Nyquist, electrical conductivity and contact impedance of the hydrogels were measured by an electrochemical workstation (CH Instruments, CHI660E). The hydrogel was coated onto the electrode sheet and allowed to equilibrate for 10 minutes prior to conducting impedance measurements over a frequency range of 0.1 to 10^6 Hz. The electrical

ARTICLE IN PRESS

conductivity was calculated by the following equation. Conductivity (S/m) = Length (m) / [Resistance (Ω) × Cross-sectional area (m^2)]. The piezoelectric responses were measured by an electrometer (Keithley 6514) and collected by a data acquisition card (NI PCI-6221), and a linear motor (LinMot H01-23 × 86/160) equipped with a force probe (M7-50, Mark-10) was employed to apply the selected pressure. sEMG signals were detected using the HPS-101 (Chengdu Taimeng Software Co., Ltd.). To mitigate motion artifacts and power-line interference, a low-pass filter (<500 Hz) and a 50 Hz notch filter within the equipment were employed. High-pass filtering (> 10 Hz) was subsequently implemented through data processing in Origin software. The SNR ($SNR = 20 \times \log_{10}(V_{signal}/V_{noise})$) was calculated from the sEMG signals, where V_{signal} represents the root-mean-square (RMS) amplitude of the EMG signal during muscle contraction, and V_{noise} represents the RMS amplitude of the baseline noise during relaxation. For SNR comparison, the PT hydrogel electrode was patterned into a circular contact area with a diameter of 10 mm, matching that of the commercial Ag/AgCl electrode. The inter-electrode distance was maintained at 2–3 cm for both electrode types. Because the same skin location cannot be occupied by both electrode types simultaneously, the PT hydrogel and commercial Ag/AgCl electrodes were tested sequentially within the same experimental session. To minimize physiological and positional variability, the electrode location was marked before testing, and the same participant, target muscle, electrode placement, amplifier settings, filtering parameters, and normal occlusion task were used for both measurements.

Numerical simulation

The stress–strain response and piezoelectric potential distribution of the serpentine-structured PVDF films were simulated using COMSOL Multiphysics. The solid mechanics and piezoelectric modules were coupled, and geometric nonlinearity was included to account for the large deformation and rotation of the serpentine bridges during tensile loading. To improve mesh quality

ARTICLE IN PRESS

and computational efficiency, the film thickness in the finite element model is increased while maintaining the aspect ratio of the planar geometry. A physics-controlled mesh was used, with local refinement applied to the serpentine bridges and island–bridge junctions. All models had the same effective length of 25 mm, while the widths corresponded to the serpentine, 2 × 3, 3 × 4, 4 × 5, and 4 × 6 structural configurations. The applied tensile strain refers to the global tensile strain imposed on the entire free-standing active region of the device. One side of the model was fixed, while a prescribed uniaxial displacement was applied to the opposite side. The free length between the two loaded boundaries was used as the reference length for calculating the applied global strain. The stress distribution shown in the Fig. is a volumetric stress distribution, with the piezoelectric potential located at the top and bottom surfaces. The PVDF material parameters were selected based on the piezoelectric material parameters in the COMSOL material library. Considering the mildly hot-pressed fibrous nature of the PVDF film and the effective compliance introduced by the island–serpentine geometry, an effective Young's modulus of 0.3 GPa was used in the mechanical simulation. For piezoelectric-potential calculation, the bottom electrode surface was electrically grounded, while the top electrode surface was assigned as the terminal boundary, allowing the simulated electric potential to represent the through-thickness potential difference generated by deformation of the PVDF sensing regions.

ARTICLE IN PRESS

Deep learning for occlusal action classification

Convolutional neural network (CNN) models were developed in Python using TensorFlow and Keras frameworks. A one-dimensional CNN (1D-CNN) architecture was employed for feature extraction and motion classification. The raw sEMG and piezoelectric signals were segmented into epochs of equal length without overlap. For each simulated occlusal action, more than 100 repeated trials were recorded, resulting in approximately 100 epochs per class. The dataset was divided into training, validation, and testing sets at a ratio of 60%, 20%, and 20%, respectively. Data splitting

ARTICLE IN PRESS

was performed at the epoch/sample level using stratified random sampling to maintain comparable class distributions among the three subsets. The validation set was used for monitoring model convergence and parameter tuning during training, whereas the testing set was held out and used only for final performance evaluation. Model training was performed using the Adam optimizer, and classification accuracy and loss were evaluated during training and validation. Convergence was typically achieved within 100 training epochs. Given the single-subject nature of the dataset, the reported accuracy reflects within-subject classification performance. All human participant testing was approved by the Institutional Review Boards of Southwest Jiaotong University, with the approval reference number of SWJTU23012-NSFC (133), and was conducted in accordance with the Declaration of Helsinki. All participants provided written informed consent before participating in the study. Because the study involved the collection and publication of identifiable images, all personally identifiable information was collected and used only after obtaining explicit, fully informed written consent from the participants. Written informed consent for the publication of identifiable images included in this article was obtained from the relevant participant(s).

Statistical Analysis

Some material characterization experiments were performed with at least three technical replicates, and quantitative data are presented as mean ± standard deviation. Statistical significance among different material groups was analyzed using one-way analysis of variance (ANOVA) in Origin software. Human surface electromyography (sEMG) and occlusal-action classification experiments were analyzed separately; the number of subjects, number of repetitions, sampling periods, and data-partitioning strategy are described in detail in the machine-learning section.

Acknowledgments

This research was financially supported by the National Natural Science Foundation of China (No. U2330120), the Beijing Key Laboratory of High-Entropy Energy Materials and Devices,

ARTICLE IN PRESS

Beijing Institute of Nanoenergy and Nanosystems (No.GS2025MS021), the Natural Science Foundation of Sichuan Province of China (No. 2026NSFSC0370), and the Basic Research Cultivation Project of Southwest Jiaotong University (No. 2682023KJ024). We are thankful for the help from the Analysis and Testing Center of Southwest Jiaotong University.

Author contributions

L.H., R.L. and W.D. conceived and designed this study. X.L. and Y.S. performed SEM observations. X.L. and Y.S. collected XRD and FTIR data. B.L., L.J. and L.H. conducted mechanical and electrical simulations. S.W. and W.Z. performed machine learning. L.H. and G.L. measured the voltage and charge output of the samples. L.H. and W.D. drafted the manuscript with contributions from all authors. W.Y. and W.D. jointly supervised this research. All authors contributed to the provided feedback on the manuscript. All authors have read and approved the final manuscript.

Competing interests

The authors declare no competing financial interests.

Data availability

The datasets generated and/or analyzed during the current study are not publicly available due to [The dataset is still being used for subsequent related research and has not yet undergone complete collation and validation to ensure its accuracy and integrity.] but are available from the corresponding author on reasonable request.

Additional information

Supplementary information The online version contains supplementary material.

Correspondence and requests for materials should be addressed to Wei Zhu, Weiqing Yang and Weili Deng.

References

1. Jin, X., et al., Assessment of occlusal force and local gas release using degradable bacterial

ARTICLE IN PRESS

cellulose/$Ti_3C_2T_x$ MXene bioaerogel for oral healthcare. *ACS Nano*, **15**, 18385-18393 (2021).

2. Du, Y., et al., Self-powered triboelectric sensor for real-time, intelligent occlusal force monitoring. *Adv. Funct. Mater.*, **36**, e19646 (2025).

3. Feng, H., et al., A fully integrated orthodontic aligner with force sensing ability for machine learning-assisted diagnosis. *Adv. Sci.*, **12**, 2411187 (2024).

4. Alqutaibi A. Y., et al., Global prevalence of temporomandibular disorders: a systematic review and meta-analysis. *J. Oral Facial Pain H.*, **39**, 48-65 (2025).

5. Song, J., et al., Polyelectrolyte-based wireless and drift-free iontronic sensors for orthodontic sensing. *Sci. Adv.*, **11**, eadu6086 (2025).

6. Stadlober, B.; Zirkl, M.; Irimia-Vladu, M., Route towards sustainable smart sensors: ferroelectric polyvinylidene fluoride-based materials and their integration in flexible electronics. *Chem. Soc. Rev.*, **48**, 1787-1825 (2019).

7. Pyo, S., et al., Recent progress in flexible tactile sensors for human-interactive systems: From sensors to advanced applications. *Adv. Mater.*, **33**, e2005902 (2021).

8. Chen, X., et al., A noise-tolerant human–machine interface based on deep learning-enhanced wearable sensors. *Nat. Sensors*, **1**, 39-51 (2026).

9. Kim, K. K., et al., A simplified wearable device powered by a generative EMG network for hand-gesture recognition and gait prediction. *Nat. Sensors*, **1**, 27-38 (2026).

10. Zhao, W., et al., Printed graphene/CNTs/TPU-fabric wearable strain sensor for healthcare monitoring. *Soft Sci.*, **5**, 10 (2025).

11. Chortos, A., et al., 3D printing of interdigitated dielectric elastomer actuators. *Adv. Funct. Mater.*, **30**, 1907375 (2020).

12. Sun, Y., Tian, G., Deng, W., Yang, W., Ionic hydrogel sensors toward next-gen personalized healthcare. Adv. Mater., 38, e09122 (2025).

13. Liu, Y.; Wang, Q., Ferroelectric polymers exhibiting negative longitudinal piezoelectric coefficient: Progress and prospects. *Adv. Sci.*, **7**, 1902468 (2020).

14. Gao, Y., et al., Advances in materials for haptic skin electronics. *Matter*, **7**, 2826-2845 (2024).

15. Wang, H., et al., A Self-Powered, Shapeable, and Wearable Sensor for Effective Hazard Prevention and Biomechanical Monitoring. *SmartSys*, **1**, e3 (2025).

16. Tian, G., et al., Hierarchical piezoelectric composites for noninvasive continuous cardiovascular monitoring. *Adv. Mater.*, **36**, e2313612 (2024).

17. Lan, B., et al., A highly sensitive coaxial nanofiber mask for respiratory monitoring assisted

ARTICLE IN PRESS

with machine learning. *Adv. Fiber Mater.*, **6**, 1402-1412 (2024).

18. Deng, W., et al., Piezoelectric nanogenerators for personalized healthcare. *Chem. Soc. Rev.*, **51**, 3380-3435 (2022).

19. Tian, G., et al., Dielectric micro-capacitance for enhancing piezoelectricity via aligning MXene sheets in composites. *Cell Rep. Phys. Sci.*, **3**, 100814 (2022).

20. Li, W., et al., Molecular ferroelectric-based flexible sensors exhibiting supersensitivity and multimodal capability for detection. *Adv. Mater.*, **33**, 2104107 (2021).

21. Tian, G., et al., A wearable all-in-one obstructive sleep apnea management system with flexible piezoelectric monitoring and soft magnetoelastic stimulating. *Matter*, **8**, 102323 (2025).

22. Wang, S., et al., Mass-produced skin-inspired piezoresistive sensing array with interlocking interface for object recognition. *ACS Nano*, **18**, 11183-11192 (2024).

23. Ji, B., et al., Localized gradient conductivity enabled ultrasensitive flexible tactile sensors with ultrawide linearity range. *Adv. Mater.*, **38**, e11275 (2026).

24. Hou, B., et al., A tactile oral pad based on carbon nanotubes for multimodal haptic interaction. *Nat. Electron.*, **7**, 777-787 (2024).

25. Li, L.; Han, L.; Hu, H.; Zhang, R., A review on polymers and their composites for flexible electronics. *Mater. Adv.*, **4**, 726-746 (2023).

26. Chen, K., et al., CoFe2O4 embedded bacterial cellulose for flexible, biodegradable, and self-powered electromagnetic sensor. *Nano Energy*, **102**, 107740 (2022).

27. Wei, Y., et al., Probing electrical double layer via triboelectric charge transfer. *Nat. Commun.*, **17**, 402 (2026).

28. Park, J., et al., Imperceptive and reusable dermal surface EMG for lower extremity neuro-prosthetic control and clinical assessment. *npj Flex. Electron.*, **7**, 49 (2023).

29. Yin, J., Wang, S., Tat, T., Chen, J., Motion artefact management for soft bioelectronics. *Nat. Rev. Bioeng.*, **2**, 541-558 (2024).

30. Wang, L., et al., All 3D-printed high-sensitivity adaptive hydrogel strain sensor for accurate plant growth monitoring. *Soft Sci.*, **5**, 2 (2025).

31. Li, X., et al., Body temperature-triggered adhesive ionic conductive hydrogels for bioelectrical signal monitoring. *Chem. Eng. J.*, **498**, 155195 (2024).

32. Wang, X., et al., Flexible iontronic pressure sensing technology: advanced structural ionic layer. *Iontronics*, **2**, 1 (2026).

33. Zhu, X., Wu, Z., Zhao, Z., Bio-inspired heterointerfacial ion-gating and iontronic

ARTICLE IN PRESS

ARTICLE IN PRESS

neuromorphics. *Iontronics*, **1**, 4 (2025).

34. Zhang, Y., et al., Enhanced photovoltaic performances of La-doped bismuth ferrite/zinc oxide heterojunction by coupling piezo-phototronic effect and ferroelectricity. *ACS Nano*, **14**, 10723-10732 (2020).

35. Ma, Y., et al., Low-dimensional van der Waals materials for linear-polarization-sensitive photodetection: materials, polarizing strategies and applications. *Mater. Futures*, **3**, 012301 (2024).

36. Xie, R., et al., A movable long-term implantable soft microfibre for dynamic bioelectronics. *Nature*, **645**, 648-655 (2025).

37. Zhang, B., et al., A three-dimensional liquid diode for soft, integrated permeable electronics. *Nature*, **628**, 84-92 (2024).

38. Lee, J., et al., Encoding of multi-modal emotional information via personalized skin-integrated wireless facial interface. *Nat. Commun.* **15**, 530 (2024).

39. Zhao, Y., et al., Ultra-conformal skin electrodes with synergistically enhanced conductivity for long-time and low-motion artifact epidermal electrophysiology. *Nat. Commun.* **12**, 4880 (2021).

40. Liu, Z., et al., A three-dimensionally architected electronic skin mimicking human mechanosensation. *Science*, **384**, 987-994 (2024).

41. Qian, X., Chen, X., Zhu, L., Zhang, Q. M., Fluoropolymer ferroelectrics: Multifunctional platform for polar-structured energy conversion. *Science*, **380**, eadg0902 (2023).

42. Chen, X., et al., Wrap-like transfer printing for three-dimensional curvy electronics. *Sci. Adv.*, **9**, eadi0357 (2023).

43. Gao, J., Niu, H., Li, Y., Li, Y., Machine-learning enabled biocompatible capacitive-electromyographic bimodal flexible sensor for facial expression recognition. *Adv. Funct. Mater*., **35**, 2418463 (2025).

44. Bai, Y., et al., Flexible strain sensors with ultra-high sensitivity and wide range enabled by crack-modulated electrical pathways. *Nano-Micro Lett.*, **17**, 64 (2025).

45. Huo, Z., et al., High-performance Sb-doped p-ZnO NW films for self-powered piezoelectric strain sensors. *Nano Energy*, **73**, 104744 (2020).

46. Yu, Q., et al., Highly sensitive strain sensors based on piezotronic tunneling junction. *Nat. Commun.*, **13**, 778 (2022).

47. Hou, B., et al., An interactive mouthguard based on mechanoluminescence-powered optical fibre sensors for bite-controlled device operation. *Nat. Electron.*, **5**, 682-693 (2022).

48. Li, S., et al., Bioresorbable, wireless, passive sensors for continuous pH measurements and

ARTICLE IN PRESS

early detection of gastric leakage. *Sci. Adv.*, **10**, eadj0268 (2024).
49. Wang, S., et al., Strain-invariant omnidirectional stretchable MXetronics. *Nat. Commun.*, **17**, 2471 (2026).
50. Yuan, Z., Shen, G., Materials and device architecture towards a multimodal electronic skin. *Mater. Today*, **64**, 165-179 (2023).
51. Zhao, H., et al., In situ structural-functional synchronous dissection of dynamic neuromuscular system via an integrated multimodal wearable patch. *Sci. Adv.*, **11**, eads1486 (2025).
52. Lu, J., et al., Hierarchically mimicking outer tooth enamel for restorative mechanical compatibility. *Nat. Commun.*, **15**, 10182 (2024).
53. Pawlaczyk, M., Lelonkiewicz, M., Wieczorowski, M. Age-dependent biomechanical properties of the skin. *Advances in Dermatology and Allergology*, **30**, 302-306 (2013).
54. Yan, Y., et al., Instantaneous self-recovery and ultra-low detection limit hydrogel electronic sensor for temporomandibular disorders intelligent diagnosis. *Nat. Commun.*, **16**, 839 (2025).
55. Busato, A., et al., Strain analysis of masseter muscle by ultrasound. *J. Biol. Reg. Homeos. Ag.*, **29**, 74-81 (2015).
56. Li, L., et al., Paintable, fast gelation, highly adhesive hydrogels for high-fidelity electrophysiological monitoring wirelessly. *Small*, **21**, 2407996 (2024).
57. Luo, J., et al., On-skin paintable water-resistant biohydrogel for wearable bioelectronics. *Adv. Funct. Mater.*, **34**, 2400884 (2024).
58. Yang, S., et al., Stretchable surface electromyography electrode array patch for tendon location and muscle injury prevention. *Nat. Commun.* **14**, 6494 (2023).

Fig. 1 Schematic of the bimodal sensing patch. a Anatomical locations of the masticatory muscles. **b** Principle of sEMG and mechanical signal acquisition. **c** Machine-learning framework for classification of occlusal states. **d** Overview of the bimodal sensing patch. **e** Simulation of stress distribution in the serpentine PVDF film (at 15% global tensile strain). **f** Hydrogel coating and **g** hydrogen-bond network reformation upon solvent evaporation. **h** Achieving adhesion at the interface between the hydrogel and skin, as well as polydimethylsiloxane. (i) Illustration of sEMG signal transduction through the hydrogel layer.

ARTICLE IN PRESS

Fig. 2 Structural design and piezoelectric characterization of the serpentine PVDF film. a Fabrication process of the serpentine PVDF film. **b** Digital photograph showing the conformal capability of the film on a curved surface. Scale bar is 5 mm. **c** Serpentine structures with different geometries but identical length and width. **d** Simulation results of stress and strain for serpentine structures of varying sizes with identical total length. **e** Electric potential distribution of the serpentine structure under tensile deformation. **f** Normalized comparison of stress, electric potential, and effective area for different structural sizes. Piezoelectric output **g** of the 2 × 3 serpentine film under different tensile strain ratios and its cyclic stability **h**. **i** Schematic illustration of the device attached at different angles. **j** Attenuation ratio of the piezoelectric output when the device is attached at different angles. **k** Average signal attenuation rate at different attachment angles.

Fig. 3 Structure and performance characterization of PT hydrogel. a Schematic of the PT hydrogen-bond network. **b** Optical images of the PT hydrogel under bending and twisting. Scale bar is 5 mm. **c** SEM image of the PT hydrogel. Scale bar is 50 μm. **d** FTIR spectra of hydrogels with varying TA content. **e** Tensile stress-strain curves of PT hydrogels with different TA concentrations. **f** Corresponding elastic modulus and elongation at break for PT hydrogels with varying TA content. **g** Weight change curve of PT hydrogel over time at 30 °C after coating. **h** Nyquist plot of PT hydrogel. **i** Ionic conductivity of PT hydrogel. **j** Schematic diagram of the mechanism enhancing hydrogel skin adhesion. **k** Comparison of adhesion between a commercial electrode and the PT hydrogel in practical applications. **l** Biocompatibility test results of PVA and PT hydrogels. Scale bars are 400 μm.

Fig. 4 Machine-learning-based classification of occlusal actions. a Schematic of electrode

ARTICLE IN PRESS

placement and corresponding muscle activation during distinct occlusion actions. **b** Optical photograph of a bimodal sensing patch. **c** Comparison of resting and active sEMG signals across different occlusal actions. **d** SNR comparison between commercial Ag/AgCl electrodes and PT hydrogel electrodes. **e** Piezoelectric responses associated with various occlusal actions. **f** Workflow diagram of machine learning. **g** Confusion matrix of occlusal-action predictions. **h** Accuracy comparison between single-modality and dual-modality inputs.

ARTICLE IN PRESS